Northumbria Research Link

Latticed-Confined Conversion Chemistry of Battery Electrode

Libin Fang[#1], Haosheng Li[#1], Ben Bin Xu[2], Jie Ma[3], Hongge Pan*[1,4], Qinggang He[5], Tianlong Zheng[5], Wenbin Ni[5], Yue Lin[6], Yangmu Li[7], Yue Cao[8,9], Chengjun Sun[8], Mi Yan*[1], Wenping Sun[1], Yinzhu Jiang*[1]

Libin Fang, Haosheng Li, Hongge Pan, Mi Yan, Wenping Sun, Yinzhu Jiang

School of Materials Science and Engineering, ZJU-Hangzhou Global Scientific and Technological Innovation Centre, Hangzhou, Zhejiang 310027, China

Email: yzjiang@zju.edu.cn

Ben Bin Xu

Mechanical and Construction Engineering, Faculty of Engineering and Environment, Northumbria University, Newcastle upon Tyne NE1 8ST, UK

Jie Ma

Key Laboratory of Artificial Structures and Quantum Control, School of Physics and Astronomy, Shanghai Jiao Tong University, Shanghai, 200240, China

Hongge Pan

Institute of Science and Technology for New Energy, Xi'an Technological University, Xi'an 710021, China

Qinggang He, Tianlong Zheng, Wenbin Ni

School of Chemical and Biological Engineering, Zhejiang University, Hangzhou, 310027 China

Yue Lin

Hefei National Research Center for Physical Sciences at the Microscale, University of Science and Technology of China, Hefei 230026, China

Yangmu Li

Beijing National Laboratory for Condensed Matter Physics, Institute of Physics, Chinese Academy of Sciences, Beijing 100190, China

Yue Cao, Chengjun Sun

Argonne National Laboratory, Lemont, Illinois 60439, USA

Yue Cao

Pritzker School of Molecular Engineering, University of Chicago, Chicago, Illinois 60637, USA

Abstract

Electrochemical conversion reaction, usually featured by multiple redox processes and high specific capacity, holds great promise in developing high-energy rechargeable battery technologies. However, the complete structural change accompanies by spontaneous atomic migration and volume variation during the charge/discharge cycle leads to electrode disintegration and performance degradation, therefore severely restrict the application of conventional conversion-type electrodes. Herein, we propose latticed-confined conversion chemistry, where the "intercalation-like" redox behaviour is realized on the electrode with a "conversion-like" high capacity. By delicately formulating the high-entropy compounds, the pristine crystal structure can be preserved well by the inert lattice framework, thus enabling an ultra-high initial Coulombic efficiency of 92.5% and a long cycling lifespan over thousand cycles after quasistatic charge-discharge cycle. This lattice-confined conversion chemistry unfolds ubiquitous insights into the localized redox reaction and sheds new lights on developing high-performance electrodes toward next-generation high-energy rechargeable batteries.

1. Introduction

Rechargeable battery technologies have been profoundly re-shaping modern life with cutting-edge energy storage solutions over the past decades[1-3], ranging from portable electronic devices, electrical vehicles to scale-up energy grids. The intercalation chemistry of electrode, represented by using graphite as anode[4] and $LiCoO_2$ as cathode[5,6], has brought great commercial successes for lithium-ion batteries (LIBs). The key of intercalation chemistry lies in the host crystal structure of electrode materials which undergo minimal change upon

lithium intercalation/deintercalation during cycling[7,8]. However, the limited theoretical capacity of intercalation-type electrode materials largely impedes the further improvement of energy density[9].

Apart from the intercalation chemistry, electrochemical conversion is another main stream electrode chemistry enabling multiple redox processes and high theoretical capacity toward high-energy rechargeable batteries, which attracts significant attention since it was firstly reported in early 2000s[10-17]. However, technical obstacles including poor reversibility[18,19] and rapid capacity fading[20] still lie in the way to make conversion-type materials a viable alternative for commercial applications. Unlike the traditional intercalation-type compounds with a stable host framework to confine redox-active atoms/cations[21-23], the enormous spontaneous atomic migration of the conversion-type electrodes in the process of phase change account for the low reversibility and rapid capacity loss during cycling[18]. From the perspective of material structure, high-entropy oxide (HEO) materials[24-28] could be a key to break this deadlock, with a homogenous distribution of electrochemical active/inactive cations and "entropy stabilization" effect of high configurational entropy[29,30]. While the HEO electrode has been demonstrated with improved integrity and enhanced cycling stability, the structural collapse seems inevitable during the lithiation of HEO electrode materials.

Herein, we propose a latticed-confined conversion chemistry enabled quasistatic charge/discharge of electrode, without explicit phase transition and structural disintegration upon charge/discharge. By utilizing the high entropy oxysulfide/oxyfluoride as electrode material, the conversion reaction can be atomically confined in the lattice framework of electrode during the whole charge/discharge processes, inheriting the "intercalation-like" redox behaviour with high initial Coulombic efficiency (ICE), full reversibility and excellent cycling stability. This latticed-confined conversion chemistry shown great potentials in

3

developing high performance battery electrode by bridging the distinct gap between the conventional conversion and intercalation chemistry.

2. Results and discussion

2.1. The Concept of 'Lattice-Confined Conversion Chemistry'

The concept of 'lattice-confined conversion chemistry' is to host the conversion reaction with a dedicated confinement to the original atomic sites during charge/discharge, which offers advantages to avoid the structural disintegration from stress localization and atomic rearrangement during the conversion reaction[31-33]. Bearing the above concept, we select high entropy oxysulfide/ oxyfluoride (HEOS/HEOF, $Mg_{0.2}Co_{0.2}Ni_{0.2}Cu_{0.2}Zn_{0.2}O(S)/(F)$) as model materials, aiming to develop "intercalation-like" redox behaviours in conversion-type electrode (Figure 1a). The HEOS/HEOF material was prepared based on a traditional solid-state method driven by high-temperature entropy at 1000 °C (Figure S1) followed by the simple sulfuration/fluorination, which uniformly incorporates three electrochemical active metal cations (Co^{2+}, Ni^{2+}, and Cu^{2+}) and two inactive metal cations (Mg^{2+} and Zn^{2+}) in a single-phase crystal structure (Figure S2, S3, S21d and S25). The two inactive metal cations are expected to hold the lattice framework during the conversion process, with the introduction of sulfur/flurine that softens/ adjusts the framework[34,35] to accommodate lattice stress and suppress atomic migration under the entropy-stabilization effect.

Rietveld refinement from a synchrotron X-ray diffraction (SXRD) pattern (Figure 1b) reveals that the as-prepared HEOS adopts a single-phase rock-salt structure indexed to a cubic lattice with space group *Fm-3m*. The introduction of sulfur results in an overall shift towards small angles compared to the reported entropy-stabilized oxides[28,36], indicating an increase in lattice parameters (Figure S4). The coordination environment of different cations in HEOS can be identified on the local atomic-scale from the Extended X-ray absorption fine structure (EXAFS) spectra result. The corresponding fitted data for each element demonstrates the

homogeneous distribution of the cations at the metal site, consistent with the structural characteristics of entropy-stabilized compounds (Figure 1c). Transmission electron microscopy (TEM) and selected area electron diffraction (SAED) patterns clearly show the (111) plane of a single rock-salt structure with a distance of 0.251 nm (Figure 1e and Figure S5). Scanning transmission electron microscope (STEM)/energy-dispersive spectroscopy (EDS) mapping exhibits that the various metal, O and S elements are all uniformly distributed over nanometre-size area (Figure 1d and Figure S6). X-ray photoelectron spectroscopy (XPS) and X-ray absorption spectroscopy (XAS) measurements suggest that all of M elements exist in the form of M^{2+} states (Figure S7). The neutron powder diffraction fitting results show that the introduced S occupies the O site (Figure S28 and Table S5). Thermogravimetric Analysis results shows that the O/S ratio in the high-entropy oxysulfide is 0.89:0.11 (Figure S29).

2.2. Electrochemical Performance

We first assess the lithium/sodium storage performance of the HEOS electrode by employing galvanostatic cycling. At a current density of 0.1 A g^{-1}, HEOS delivers the initial discharge/charge capacities of 830 mA h g^{-1} and 753 mA h g^{-1} for lithium-ion batteries and discharge/charge capacities of 641 mA h g^{-1} and 581 mA h g^{-1} for sodium-ion batteries, corresponding to high ICE of 90.6% and 90.7% respectively (Figure 2a,b and S8). Given the inevitable capacity loss induced by the formation of the solid electrolyte interface (SEI)[37], the above ICE unveils almost full reaction reversibility for HEOS. The rate capability for sodium-ion batteries is also quite impressive with the capacity of 211 mA h g^{-1} recorded at a high current density of 5.0 A g^{-1} (Figure S9b,c). Most interestingly, a high capacity of 375 mA h g^{-1} is maintained at 0.5 A g^{-1} after 1500 cycles with a high capacity retention of 81.2%, while a higher capacity retention of 84.9% can be achieved at a high current density of 1.0 A g^{-1} up to 1500 cycles (Figure 2e and Figure S10). In the absence of carbon composite and topography

design (Figure S11a,b), such excellent ICE and cycling stability of HEOS already make HEOS stand out as a competitive candidate, even more promising than those conversion-type electrodes with a delicate design of components and structures (Figure S12). By comparison, the ICE and cyclic stability of the electrode materials composed of HEO, single cation (NiO(S) and CoO(S)) with the same rock-salt structure and multiple-phase composite with the same composition as HEOS are substantially worse (Figure 2e and Figure S13) due to the absence of lattice-confined conversion reaction.

We next investigate the feasibility to bring these electrochemical behaviors to micrometer-sized particles, which tend to experience less decomposition of the electrolyte compared to nano-sized particles and benefits for practical applications. Despite the slight reduction of capacities, the HEOS electrode with an average size of ~2 μm (Figure S11c,d) delivers a high ICE of 92.5% (Figure 2c), due to the decreased irreversible capacity loss induced by the formation of SEI[38-40]. Moreover, the micrometer-sized HEOS electrode exhibits excellent capacity retention of 87.4% over 1000 cycles at 0.5 A g^{-1}, with an average CE higher than 99.5% (Figure S14). The lithium storage performance of HEOF (Figure S15) further confirm the high reaction reversibility and excellent cycle stability. Benefiting from the lattice-confined conversion reaction, HEOS/HEOF exhibits much higher initial Coulombic efficiency (Figure 2d and Figure S16) and cycling stability compared with high-entropy oxides with the same crystal structure.

To demonstrate the possibility for practical application, full cells based on Na$_3$V$_2$(PO$_4$)$_3$/C cathode and HEOS anode are assembled, where the Na$_3$V$_2$(PO$_4$)$_3$ is selected as the pairing cathode for its specific electronic structure and attractive crystal features consisting of open channels for rapid Na$^+$ diffusion[41]. The Na$_3$V$_2$(PO$_4$)$_3$/C delivers a stable capacity of ~90 mA h g^{-1} in a half cell at 0.5 A g^{-1} (Figure S17a,b). As for the sodium storage performance of the full

cell, a high reversible capacity of 490 mA h g^{-1} and a moderate output voltage of 2.0 V are presented at a current density of 0.5 A g^{-1}, with an excellent capacity retention of 85.5% over 150 cycles (Figure S17c,d).

2.3. Structure and Chemical Environmental Evolution

The structural evolution upon sodiation/desodiation is investigated by utilizing *in-situ* synchrotron XRD. Surprisingly, the (111) and (200) reflections of the rock-salt structure exist in the whole sodiation/desodiation process, with only reversible shift recorded corresponding to the volume change of unit cell (Figure 3a). Such results are obviously distinct from the structure collapse of traditional conversion electrodes and previously reported high-entropy oxide anodes[27], but have more "intercalation-type" characteristics[33,42,43]. The structural stability of high-entropy oxysulfide undoubtedly contributes to the excellent cycling stability and reversibility upon the conversion reaction occurs.

The redox behavior in the HEOS electrode was evaluated by *ex situ* XPS and EELS analyses to capture the changes of *M* electronic states. For Mg and Zn elements which are the leading building blocks to preserve the lattice framework upon cycling, the peaks of Mg 2p and Zn 2p remain consistent with the fresh state at the discharged and charged states, suggesting the inertial behavior of Mg and Zn element during sodiation/desodiation (Figure S18a,b). Compared to the fresh state, the peaks of Cu, Co and Ni elements shift toward lower binding energy, indicating the reduction of Cu^{2+}, Co^{2+} and Ni^{2+} to Cu^0, Co^0 and Ni^0, respectively (Figure S18d-f). By analyzing the L edges of Cu, Co and Ni in the fresh, discharged and charged states in the EELS spectra (Figure S19), the intensity of both L$_3$ and L$_2$ edges of the discharged state significantly decreases with the greater 3d-state occupancy of the metallic state[44]. In addition, the shift of the peaks of Cu towards higher energy loss, the new shoulder peaks appearing at 789.5 eV in L$_3$ edge of Co and 865 eV in L$_3$ edge of Ni show the signal characteristics of Cu^0,

Co[0], and Ni[0], respectively[45,46]. In combination with *ex-situ* XPS and EELS at the discharged state, it reveals that these three elements undergo the conversion reaction to contribute the capacity. After re-charging, all three metal elements shift back to their initial energy positions, indicating good reversibility of the metal redox.

Ex-situ synchrotron XAS analysis was further conducted to explore the local structure evolution during cycling. The X-ray absorption near-edge structures (XANES) of the K-edge of Zn, Ni, Cu of HEOS at pristine, fully-sodiated and fully-desodiated states, respectively are displayed in Figure 3b-d and Figure S20. The Zn K-edge in three states keeps unchanged while Ni and Cu K-edge show a significant shift to low energy in the discharge state, indicating again that the valence state of the Zn element remains unchanged and Co, Ni elements are reduced during sodiation process. On the other hand, the EXAFS and corresponding fitting results of K-edge clearly show a local chemical environment change different from the conventional conversion-type electrode material (Tab. S1-S3). From pristine to fully-sodiated state, regardless of whether it is an active element or an inactive element, the coordination number of the first coordination shell corresponding to the *M*-O bond does not completely disappear but only slightly decreases, which confirms the preservation of the local chemical environment corresponding to the original structural skeleton. On the second coordination shell that mainly consists of transition metal atoms, the significant decline of the coordination number indicates that these active metal atoms are involved in redox reactions that cause *M*-O bond to break, especially the second coordination shell of Cu is transformed into the characteristic bond length of Cu alloy.

The above structural and element tracing results consolidate and portray our unique concept of 'lattice-confined conversion reaction' (Figure 3h). When the conversion reaction occurs, it is restricted by the local framework constructed by inactive elements. Except for the

short-range migration of copper, which possesses more migration ability[47], other active elements are constrained at the atomic scale and redox reactions are performed with this confinement. The unique 'lattice-confined' characteristics provide structural merit for the subsequent charging to fully reversible recovery of the pristine lattice framework of the rock-salt phase. In Figure 3e-g, it can be clearly evidenced that the HEOS electrode after charging exhibits features similar to the pristine state in the local range of 1-4 Å. The first and second neighbours of Zn, Cu, Ni elements after desodiation keep consistent with those in the pristine state, indicating that the redox-active metal atoms involved in the conversion reaction return to the initial position of the lattice.

2.4. Atom Re-arrangement and Phase Transition upon Cycling

We next track the atomic locations and map the phase transition of the sodiation/desodiation process to further understand the underlying mechanism of reversible sodium storage by using HAADF-STEM, HRTEM, SAED and FFTS (Figure S21 and Figure S22). The initial rock-salt structure is still clearly preserved except for the slight increase from 0.144 to 0.148 nm of (300) (Figure 4a-c) and 0.251 to 0.260 nm of (111) plane lattice spacing (Figure S22a-c), which is in good agreement with the in-situ XRD results. To further compare the statistics of interplanar spacing (Figure 4d,e and Figure S22d,e), both the pristine and fully charged HEOS exhibit uniform crystal plane distribution, while the fully sodiation state shows significant fluctuations, which can be considered to be due to the adaptive distortion of the soft lattice caused by sodiation. From the micro area of HEOS at fully-sodiated state observed with HRTEM and FFTS (Figure S22i-l), it appears that the salt rock structure diffraction spots coexist with new diffraction spots indexed to (200) plane of Cu-Ni alloy/ Cu metal and (311) plane of Na_2O within a few nanometer scales. The intensity profiles (Figure 4j,k) along the white rectangle shows the overall characteristics of the (111) crystal plane "inlaid" with

significant deviations from the original lattice spacing at several atomic scales, which agree well with the (311) plane of Na_2O and (200) plane of alloy. The magnified image on the selected area in Figure 4f-g, suggests that the 1-2 nm square region with different orientations appears in the rhomboid lattice frame along the zone axis [01$\bar{1}$]. Comparing the corresponding FFTs of ROI4 and ROI5 (Figure 4h,i), the square region with different orientations is likely to associate with new diffraction spots of (200) plane of alloy.

From the above HRTEM, HAADF and FFTS results, ==the original rock salt structure serves as a stable framework to limit the zero-valent metal/alloy and Na_2O of the conversion products== to a few atomic scales, during the 'lattice-confined' conversion reaction. It appears that the above-mentioned unique behavior could facilitate the complete reoccupation of the previously reduced cations to their initial sites of the HEOS lattice during the subsequent desodiation process. Indeed, the HRTEM image (Figure S21o-q) reveals that atomic-scale reaction products completely disappeared and reverted back to the original rock-salt structure at the fully desodiated state, which is also validated by the SAED pattern (Figure S22f-h). The EDS results rule out any segregation of elements and possible changes in the elemental composition of the HEOS electrode after charging (Figure S21r), which is consistent with the pristine state. These findings suggest that a fully reversible conversion reaction is realized in the HEOS electrode. In addition, a similar reversible uniform distribution can also be observed in the EDS results of HEOF (Figure S25, S26 and S27), indicating its potential lattice-confined conversion reaction capability.

When the conversion reaction performs with large amount of sodium, the energy state of the crystal framework should be boosted which can be reflected from the change in the stress state. The internal stress concentration remains as a major driving force for the collapse of structure and the phase transition[48,49]. Combined with geometric phase analysis, we find that

the lattice stress in the discharged state is significantly higher than that in the initial state and the charged state (Figure S23), and there is a certain degree of lattice distortion and twin crystals generation (Figure 4l, Figure S21e-h, j-l and Figure S24). Based on the mechanical enhancement mechanism of twins in high entropy alloys and metals as reported[50,51], we believe that twin crystals achieve spontaneous structural adjustment and stress relief through a plastic deformation mechanism inside the discharged HEOS electrode (Tab. S4). As such, the coexistence of the huge internal stress caused by large sodium/lithium storage capacity and the stable crystal lattice existing in the lattice-confined conversion reaction can be well explained. First, the softening of crystal lattice by anionic sulfur extends the tolerance to internal stress; second, the huge stress can be released by expanding the lattice spacing and generating twin crystals.

By now, the mechanism of 'lattice-confined conversion reaction' has been completely unfolded. Within the lattice, the Zn and Mg elements serve as an "intercalation-like" matrix to stabilize the initial structural framework rather than participate in redox reactions, while sodiation induces conversion reactions of other cations (e.g., Cu^{2+}, Co^{2+}, and Ni^{2+}) to realize high capacity. Unlike the conventional conversion reactions, the high entropy feature of HEOS electrode results in a disordered arrangement of metal atoms in the structure, wherein the enormous migration of redox-active atoms is greatly hindered by the high-entropy cation disordered frame structure, that is, the reduced zero-valent metal atom remain "trapped" inside the lattice of HEOS. During the desodiation process, the generated atomic conversion products can comfortably recover to the original state, thereby achieving complete reversibility and obtaining high ICE. Besides, the 'lattice-confined conversion reaction' mechanism ensures the stable existence of the initial phase structure throughout the entire electrochemical reaction process and releases the huge stress caused by the conversion

reaction through moderate local structural adjustment, leading to outstanding cyclic stability. A similar result has been validated with Li$^+$, where the presence of 'lattice-confined conversion reaction' enables an excellent electrochemical performance of HEOS and HEOF.

3. Conclusion

Based on the concept of 'lattice-confined conversion reaction', we develop a robust electrode strategy by utilizing the high-entropy oxysulfide materials, and successfully achieve the high-capacity multi-electron conversion reaction and structural integrity during long-term cycling. Microscopically, the electrochemical reaction process of HEOS presents a robust and resilience performance as the intercalation reaction, where the active metal element in the stress-adaptive lattice undergoes the conversion reaction to realize high capacity. Benefitted from the unique lattice-confined conversion reaction, the exemplified HEOS electrode delivers the high ICE of 90.7% and up to 1500 stable cycles with the capacity retention of 84.9%, as well as 1000 stable cycles (capacity retention of 87.4%) and higher ICE of 92.5% even in micrometer-size. The corresponding structural motifs are clearly revealed to realize the lattice-confined conversion reaction chemistry. We expect that the proposed lattice-confined conversion reaction would provide new ideas and insights for solving the intrinsic issues of conversion-type electrodes.
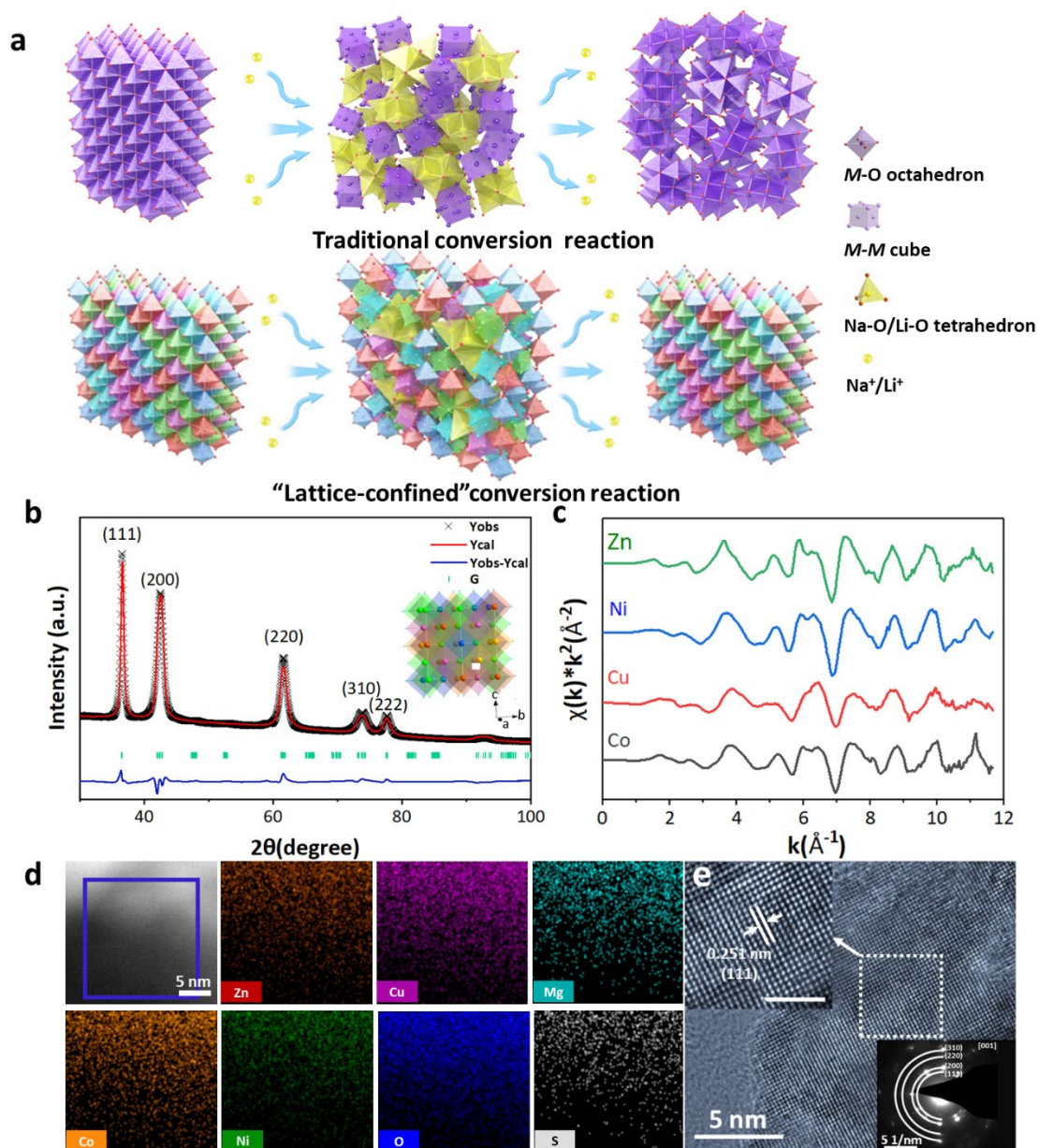
Figure 1. 'Lattice-confined conversion chemistry' of battery electrode and characterization of high entropy oxysulfide. a) Schematic diagram of the 'lattice-confined' conversion reaction process. The figure shows that the traditional "conversion-type" electrode material undergoes a complete transformation of the phase structure during the process of lithium/sodium storage, which causes the structure to collapse during the cycle process. b) Rietveld refinement from a synchrotron X-ray diffraction (SXRD) pattern which corresponds well to the salt rock structure with slightly increased lattice parameters. c) EXAFS spectra of HEOS, which shows a similar neighboring chemical environment, indicating that it is consistent with the "high entropy" element uniform spatial distribution characteristics. d,e) HAADF-STEM EDS mapping images and HRTEM image. The diffraction pattern is recorded parallel to the [001] direction of the crystal.
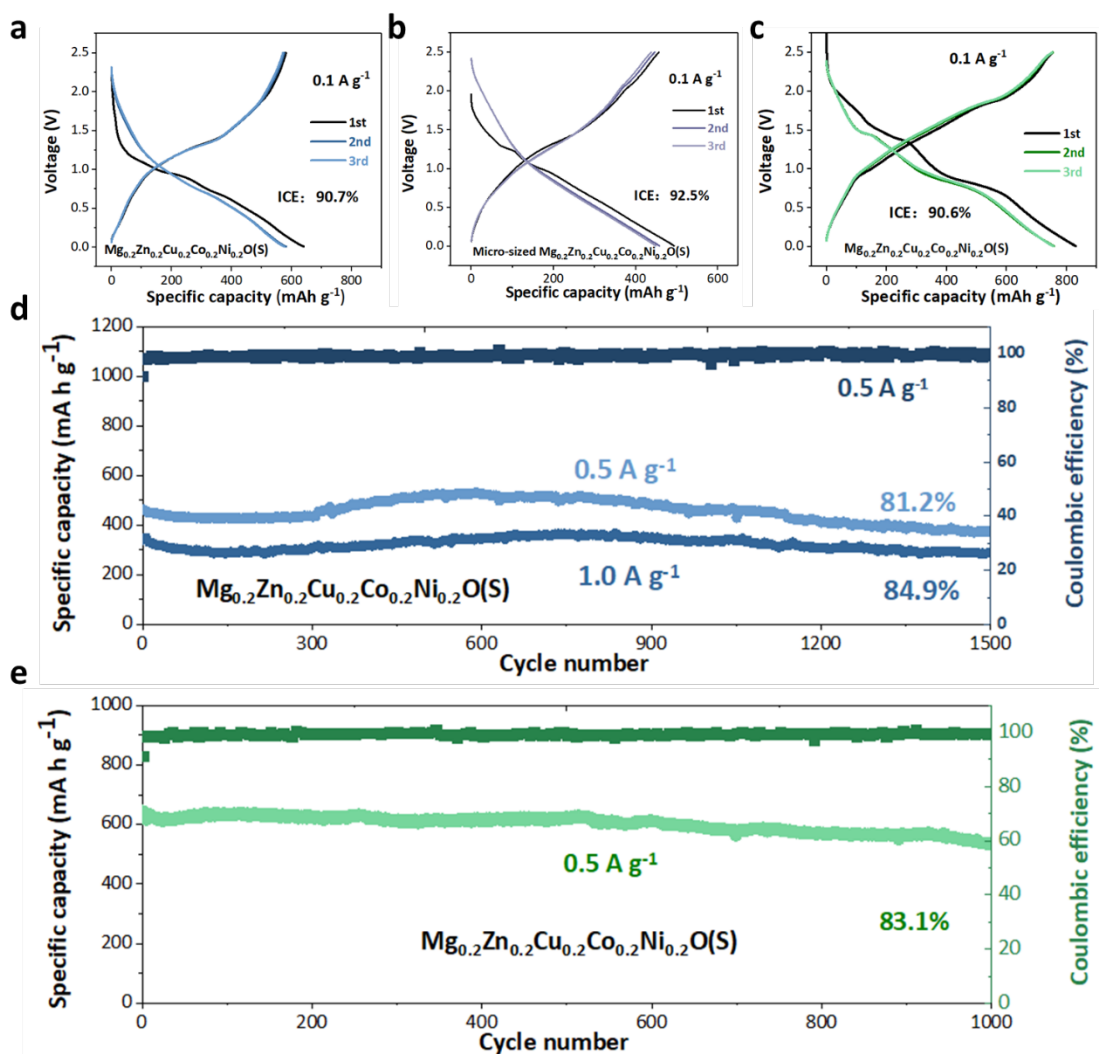
Figure 2. Electrochemical performance of HEOS. a) Galvanostatic discharge-charge curves of the HEOS electrode at a current density of 0.1 A g⁻¹ in the voltage range of 0.01-2.5 V (vs. Li/Li⁺), which shows a high initial Coulombic efficiency of 90.6%. Galvanostatic discharge-charge curves of b) the nano-sized HEOS and c) micro-sized HEOS electrode at a current density of 0.1 A g⁻¹ in the voltage range of 0.01-2.5 V (vs. Na/Na⁺), which shows a high initial Coulombic efficiency of 92.5% for micro-sized HEOS as well. d) Cycling performance comparison of HEOS and HEO for lithium-ion batteries. It can be seen that the introduction of S can significantly improve initial Coulomb efficiency and cycle stability. e) The cycling performance of HEOS is compared with HEO, CoO(S), NiO(S) and composite for Na-ion batteries, among which HEOS exhibits the highest initial Coulombic efficiency and cycling stability.
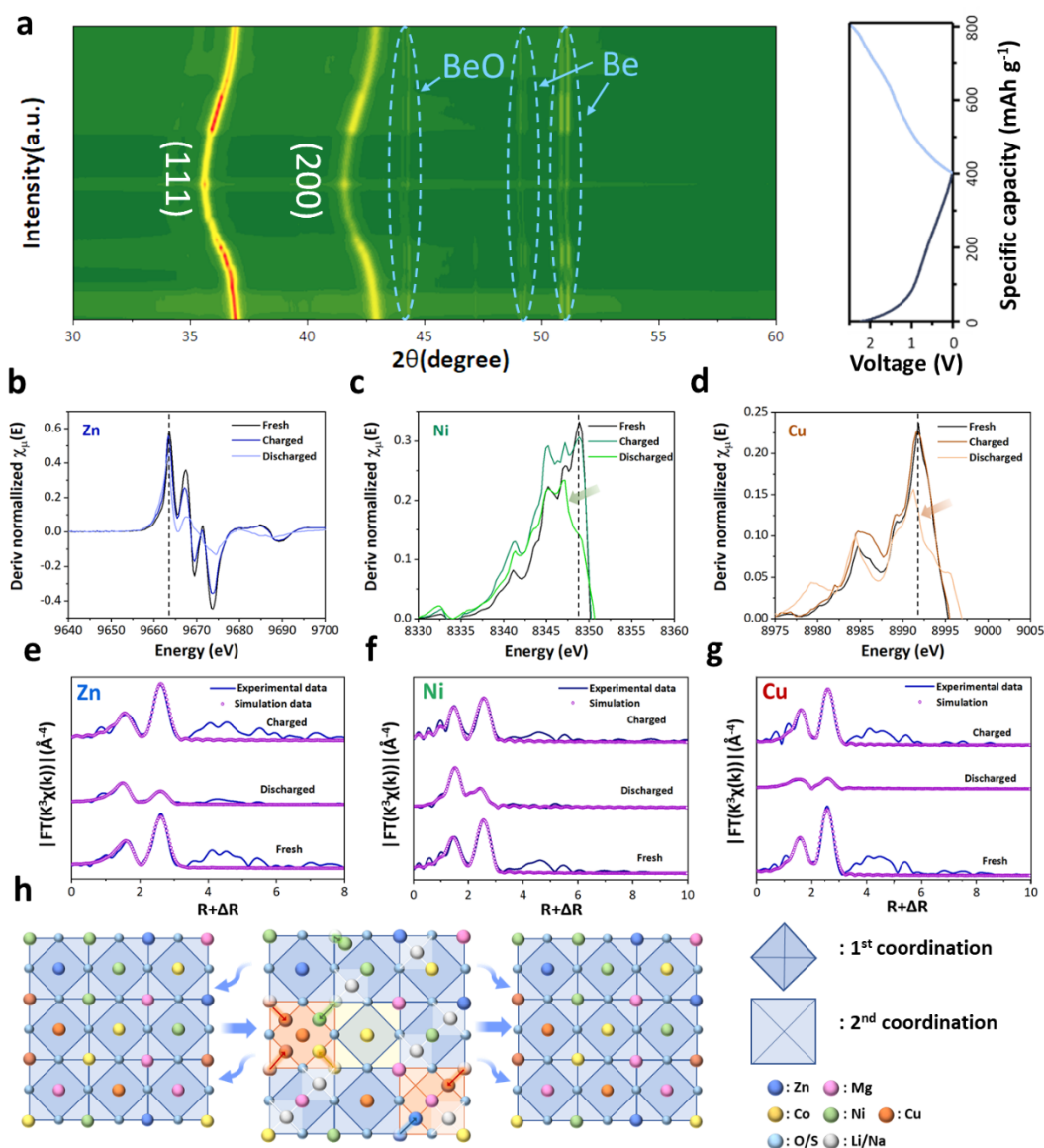
Figure 3. Phase structure and chemical environment. a) In-situ synchrotron XRD patterns of HEOS electrode during charge/discharge processes, in which the (111) and (200) peaks of the salt rock structure exist stably during the charge-discharge reaction process. b-d) Derivative XANES spectra of HEOS at the fresh, discharged and charged states. The chemically inert Zn has no change in the valence state, while the chemically active Ni and Cu have a significant blue shift in the discharged state. e-g) EXAFS spectra and fitting results of Zn, Ni and Cu at the fresh, discharged and charged states. h) Schematic diagram of the development of coordination environment during the 'lattice-confined' conversion reaction process.
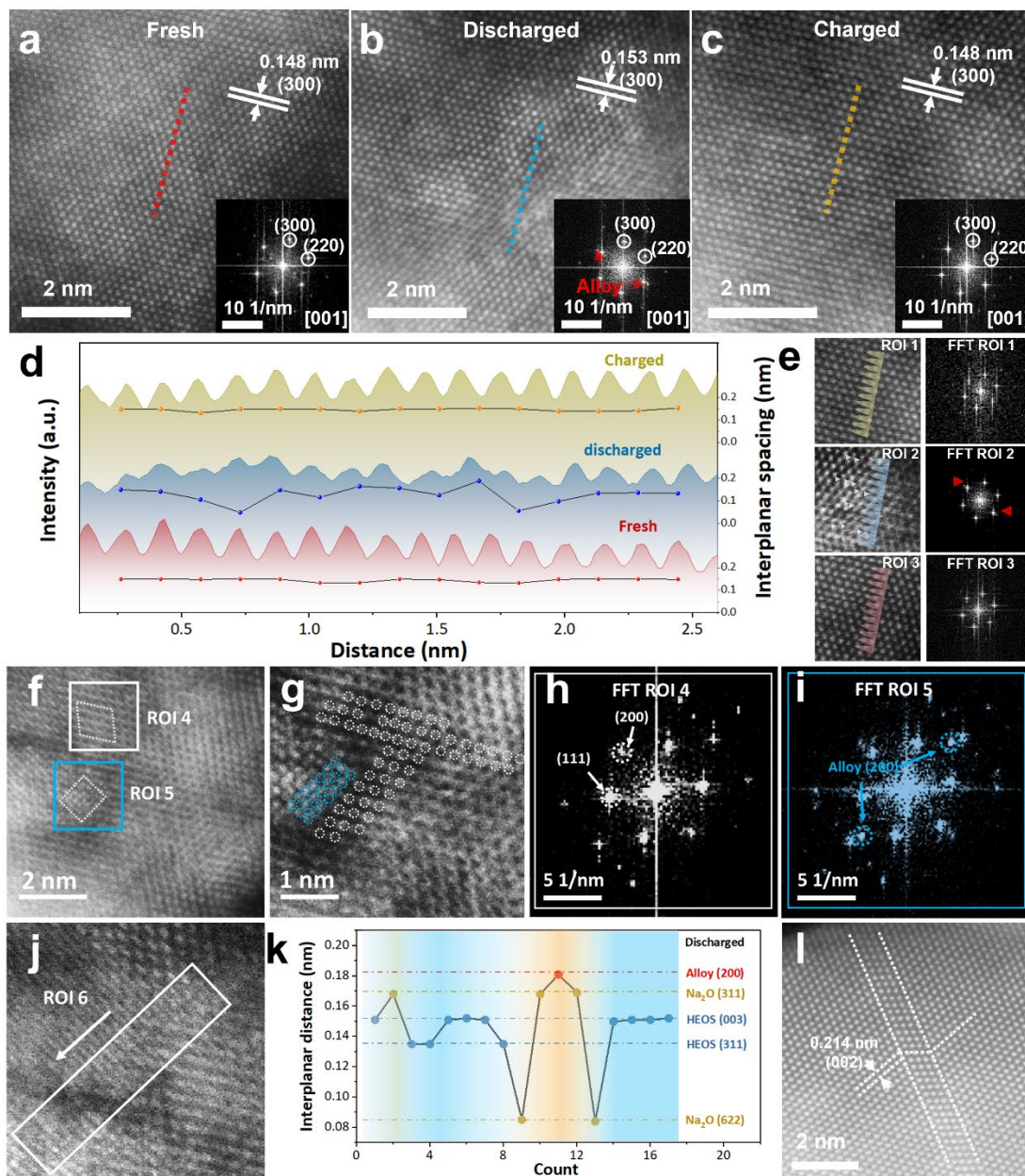
Figure 4. Atom arrangement and phase transition. a-c) HAADF-STEM images of the HEOS at the fresh, discharged and charged states, which show the same crystal framework of the salt rock structure. d) Intensity profile along the red, blue and yellow lines revealing a periodic variation in contrast. It shows that the interplanar spacing is uniform in the fresh and charged state, which can be observed in further by HRTEM in e), while the discharged state has new small intensity fluctuations between the crystal planes, exhibiting the phenomenon of "intercalation". f-j) Partial magnification of HRTEM images and responding FFT of the HEOS at the discharged state, k) Intensity profile along with the white rectangle in ROI 6. l) HRTEM image of HEOS at the discharged state shows the crystal twin.

WILEY-VCH

Received: ((will be filled in by the editorial staff))
Revised: ((will be filled in by the editorial staff))
Published online: ((will be filled in by the editorial staff))

References

[1]   D. Larcher, J. M. Tarascon, *Nat. Chem.* **2015**, 7, 19-29.

[2]   N. Nitta, F. Wu, J. T. Lee, G. Yushin, *Mater. Today* **2015**, 18, 252-264.

[3]   J. W. Choi, D. Aurbach, *Nat. Rev. Mater.* **2016**, 1, 16013.

[4]   D. Guerard, A. Herold, *Carbon* **1975**, 13, 337-345.

[5]   K. Mizushima, P. C. Jones, P. J. Wiseman, J. B. Goodenough, *Mater. Res. Bull.* **1980**, 15, 783-789.

[6]   J. M. Tarascon, M. Armand, *Nature* **2001**, 414, 359-367.

[7]   J. B. Goodenough, K.-S. Park, *J. Am. Chem. Soc.* **2013**, 135, 1167-1176.

[8]   H. Liu, Z. Zhu, Q. Yan, S. Yu, X. He, Y. Chen, R. Zhang, L. Ma, T. Liu, M. Li, R. Lin, Y. Chen, Y. Li, X. Xing, Y. Choi, L. Gao, H. S.-Y. Cho, K. An, J. Feng, R. Kostecki, K. Amine, T. Wu, J. Lu, H. L. Xin, S. P. Ong, P. Liu, *Nature* **2020**, 585, 63-67.

[9]   Q. Liu, X. Su, D. Lei, Y. Qin, J. Wen, F. Guo, Y. A. Wu, Y. Rong, R. Kou, X. Xiao, F. Aguesse, J. Bareño, Y. Ren, W. Lu, Y. Li, *Nat. Energy* **2018**, 3, 936-943.

[10]   S. L. P. Poizot, S. Grugeon, L. Dupont & J-M. Tarascon, *Nature* **2000**, 407, 496-499.

[11]   J. Cabana, L. Monconduit, D. Larcher, M. R. Palacin, *Adv. Mater.* **2010**, 22, E170-92.

[12]   M. Chen Yu, Y. Yu Xin, Z. Li, U. Paik, W. Lou Xiong, *Sci. Adv.* **2016**, 2, e1600021.

[13]   B. Wu Hao, W. Lou Xiong, *Sci. Adv.* **2017**, 3, eaap9252.

[14]   Y. Jiang, Y. Li, W. Sun, W. Huang, J. Liu, B. Xu, C. Jin, T. Ma, C. Wu, M. Yan, *Energy Environ. Sci.* **2015**, 8, 1471-1479.

[15]   L. Fang, C. Wang, L. Huangfu, N. Bahlawane, H. Tian, Y. Lu, H. Pan, M. Yan, Y. Jiang, *Adv. Funct. Mater.* **2019**, 29, 1906680.

[16]   L. Fang, Z. Lan, W. Guan, P. Zhou, N. Bahlawane, W. Sun, Y. Lu, C. Liang, M. Yan, Y. Jiang, *Energy Stor. Mater.* **2019**, 18, 107-113.

[17]   L. Fang, N. Bahlawane, W. Sun, H. Pan, B.B. Xu, M. Yan, Y. Jiang, *Small* **2021**, 17, 2101137.

[18]   L. Li, R. Jacobs, P. Gao, L. Gan, F. Wang, D. Morgan, S. Jin, *J. Am. Chem. Soc.* **2016**, 138, 2838-2848.

[19]   X. Hua, A. S. Eggeman, E. Castillo-Martínez, R. Robert, H. S. Geddes, Z. Lu, C. J. Pickard, W. Meng, K. M. Wiaderek, N. Pereira, G. G. Amatucci, P. A. Midgley, K. W. Chapman, U. Steiner, A. L. Goodwin, C. P. Grey, *Nat. Mater.* **2021**, 20, 841-850.

[20]   J. Li, S. Hwang, F. Guo, S. Li, Z. Chen, R. Kou, K. Sun, C.-J. Sun, H. Gan, A. Yu, E. A. Stach, H. Zhou, D. Su, *Nat. Commun.* **2019**, 10, 2224.

[21]   M. S. Whittingham, *Chem. Rev.* **2004**, 104, 4271-4302.

[22]   L. Croguennec, M. R. Palacin, *J. Am. Chem. Soc.* **2015**, 137, 3140-3156.

[23]   D.-H. Seo, J. Lee, A. Urban, R. Malik, S. Kang, G. Ceder, *Nat. Chem.* **2016**, 8, 692-697.

[24]   P. Ghigna, L. Airoldi, M. Fracchia, D. Callegari, U. Anselmi-Tamburini, P. D'angelo, N. Pianta, R. Ruffo, G. Cibin, D. O. De Souza, E. Quartarone, *ACS Appl. Mater. Interfaces* **2020**, 12, 50344-50354.

[25]   N. Qiu, H. Chen, Z. Yang, S. Sun, Y. Wang, Y. Cui, *J. Alloys Compd.* **2019**, 777, 767-774.

[26]   A. Sarkar, L. Velasco, D. Wang, Q. Wang, G. Talasila, L. De Biasi, C. Kübel, T. Brezesinski, S. S. Bhattacharya, H. Hahn, B. Breitung, *Nat. Commun.* **2018**, 9, 3400.

[27]   A. Sarkar, Q. Wang, A. Schiele, M. R. Chellali, S. S. Bhattacharya, D. Wang, T. Brezesinski, H. Hahn, L. Velasco, B. Breitung, *Adv. Mater.* **2019**, 31, 1806236.

[28]   C. M. Rost, E. Sachet, T. Borman, A. Moballegh, E. C. Dickey, D. Hou, J. L. Jones, S. Curtarolo, J.-P. Maria, *Nat. Commun.* **2015**, 6, 8485.

[29]   F. Otto, Y. Yang, H. Bei, E. P. George, *Acta Mater.* **2013**, 61, 2628-2638.

[30]   N. G. Jones, J. W. Aveson, A. Bhowmik, B. D. Conduit, H. J. Stone, *Intermetallics* **2014**, 54, 148-153.

[31]   Y. Sun, N. Liu, Y. Cui, *Nat. Energy* **2016**, 1, 16071.

[32]   J. Wang, L. Wang, C. Eng, J. Wang, *Adv. Energy Mater.* **2017**, 7, 1602706.

[33]   S. Fang, D. Bresser, S. Passerini, *Adv. Energy Mater.* **2020**, 10, 1902485.

[34]   P. Geng, S. Zheng, H. Tang, R. Zhu, L. Zhang, S. Cao, H. Xue, H. Pang, *Adv. Energy Mater.* **2018**, 8, 1703259.

[35]   F. Zhao, J. Liang, C. Yu, Q. Sun, X. Li, K. Adair, C. Wang, Y. Zhao, S. Zhang, W. Li, S. Deng, R. Li, Y. Huang, H. Huang, L. Zhang, S. Zhao, S. Lu, X. Sun, *Adv. Energy Mater.* **2020**, 10, 1903422.

[36]   Y. Sun, S. Dai, *Sci. Adv.* **2021**, 7, eabg1600.

[37]   H. Wu, G. Chan, J. W. Choi, I. Ryu, Y. Yao, M. T. Mcdowell, S. W. Lee, A. Jackson, Y. Yang, L. Hu, Y. Cui, *Nat. Nanotechnol.* **2012**, 7, 310-315.

[38]   R. Hu, D. Chen, G. Waller, Y. Ouyang, Y. Chen, B. Zhao, B. Rainwater, C. Yang, M. Zhu, M. Liu, *Energy Environ. Sci.* **2016**, 9, 595-603.

[39]   H. Song, J. Su, C. Wang, *Adv. Energy Mater.* **2019**, 9, 1900426.

[40]   B. Zhu, G. Liu, G. Lv, Y. Mu, Y. Zhao, Y. Wang, X. Li, P. Yao, Y. Deng, Y. Cui, J. Zhu, *Sci. Adv.* **2019**, 5, eaax0651.

[41]   Z. Jian, W. Han, X. Lu, H. Yang, Y.-S. Hu, J. Zhou, Z. Zhou, J. Li, W. Chen, D. Chen, L. Chen, *Adv. Energy Mater.* **2013**, 3, 156-160.

[42]   F. Wu, G. Yushin, *Energy Environ. Sci.* **2017**, 10, 435-459.

[43]   Y. Li, Y. Lu, P. Adelhelm, M.-M. Titirici, Y.-S. Hu, *Chem. Soc. Rev.* **2019**, 48, 4655-4687.

[44]   E. C. Dickey, V. P. Dravid, P. D. Nellist, D. J. Wallis, S. J. Pennycook, A. Revcolevschi, *Microsc. Microanal.* **1997**, 3, 443-450.

[45]   L. Laffont, M. Y. Wu, F. Chevallier, P. Poizot, M. Morcrette, J. M. Tarascon, *Micron* **2006**, 37, 459-464.

[46]   Y. Zhao, T. E. Feltes, J. R. Regalbuto, R. J. Meyer, R. F. Klie, *J. Appl. Phys.* **2010**, 108, 063704.

[47]   F. Wang, R. Robert, N. A. Chernova, N. Pereira, F. Omenya, F. Badway, X. Hua, M. Ruotolo, R. Zhang, L. Wu, V. Volkov, D. Su, B. Key, M. S. Whittingham, C. P. Grey, G. G. Amatucci, Y. Zhu, J. Graetz, *J. Am. Chem. Soc.* **2011**, 133, 18828-18836.

[48]   M. Mao, A. Nie, J. Liu, H. Wang, S. X. Mao, Q. Wang, K. Li, X.-X. Zhang, *Nanotechnology* **2015**, 26, 125404.

[49]   H. Tavassol, M. W. Cason, R. G. Nuzzo, A. A. Gewirth, *Adv. Energy Mater.* **2015**, 5, 1400317.

[50]   Z. An, S. Mao, Y. Liu, H. Zhou, Y. Zhai, Z. Tian, C. Liu, Z. Zhang, X. Han, *J. Mater. Sci. Technol.* **2021**, 92, 195-207.

[51]   S. Zhao, R. Zhang, Q. Yu, J. Ell, O. Ritchie Robert, M. Minor Andrew, *Science* **2021**, 373, 1363-1368.

Latticed-Confined Conversion Chemistry of Battery Electrode

Libin Fang[#], Haosheng Li[#], Ben Bin Xu, Jie Ma, Hongge Pan*, Qinggang He, Tianlong Zheng, Wenbin Ni, Yue Lin, Yangmu Li, Yue Cao, Chengjun Sun, Mi Yan*, Wenping Sun, Yinzhu Jiang*

Latticed-confined conversion chemistry is proposed and realized assisted with "high-entropy" electrode, enabling long cycling life-span and ultra-high initial Coulombic efficiency, where the "intercalation-like" redox behavior is realized on the electrode with a "conversion-like" high capacity. We further reveal stress-releasing mechanisms such as lattice expansion and twinning strengthening of crystal frameworks constructed by inactive elements.

ToC figure:

"Rock-salt" structure   conversion   disintegration

M-O octahedron
M-*M* cube
Na-O/Li-O tetrahedron
Na⁺/Li⁺

"high-entropy"   "lattice-confined" conversion   stable structural frame